Cloud-Based Multispectral Analysis for Mapping Hydrothermal Alteration Zones in Zamfara State, Nigeria

Taiwo Olatunji Qudus[1], Muhammad Rabiu Dahiru [2] Abdullahi Mohammed Salihu [3]
Aduojo Atakpa [4]
[1,2,3,4] *National Space Research and Development Agency (NASRDA), Abuja, Nigeria*

Abstract—**Hydrothermal alteration mapping is a critical step in mineral exploration reconnaissance, particularly in geologically complex terrains such as the Nigerian Basement Complex. This study applies cloud-based multispectral remote sensing techniques to map and characterize hydrothermal alteration zones in Zamfara State, northwestern Nigeria, using Advanced Spaceborne Thermal Emission and Reflection Radiometer (ASTER) imagery processed within the Google Earth Engine (GEE) platform. Dry-season ASTER data were atmospherically corrected using the Dark Object Subtraction (DOS) technique, and targeted band ratio expressions were applied to delineate eleven diagnostic mineral assemblages, including Al-OH minerals (kaolinite, illite-muscovite, montmorillonite, alunite-pyrophyllite), iron oxides and hydroxides (hematite, goethite, jarosite), carbonate and Mg-OH minerals (chlorite, epidote), as well as silica (quartz) and sulfate (gypsum) phases. Results reveal a well-defined spatial zonation of alteration assemblages, with argillic and phyllic minerals (kaolinite, illite-muscovite, jarosite, goethite) concentrated in the southern Maru region associated with the Anka and Maru schist belts, while propylitic assemblages (carbonates, Mg-OH minerals) dominate the northern and central zones. This systematic alteration zoning is consistent with a preserved hydrothermal system suggestive of porphyry copper and epithermal gold environments. The derived mineral maps were validated against existing geological maps and known mineralization occurrences, confirming their spatial coherence with documented schist belt geology. The study demonstrates the effectiveness of Google Earth Engine-hosted ASTER analysis as a cost-efficient, scalable reconnaissance tool for targeting high potential zones in underexplored regions of the West African Craton.**

Index Terms—**ASTER, hydrothermal alteration, Google Earth Engine, mineral mapping, band ratios,**

I. INTRODUCTION

Mineral exploration has been significantly advanced by the integration of satellite remote sensing, with the Advanced Spaceborne Thermal Emission and Reflection Radiometer (ASTER) serving as a primary tool for regional lithological mapping and hydrothermal alteration detection. Unlike conventional optical sensors, ASTER's unique configuration of fourteen spectral bands specifically its six shortwave infrared (SWIR) and five thermal infrared (TIR) channels enables the identification of diagnostic absorption features associated with Al-OH, Mg-OH, carbonate, and silicate mineral groups. The Advanced Spaceborne Thermal Emission and Reflection Radiometer (ASTER) has emerged as a pivotal tool in mineral exploration, offering multispectral capabilities that enable the detection of hydrothermal alteration zones and lithological mapping across diverse geological terrains.

Recent studies have demonstrated that ASTER data, when integrated with complementary datasets and advanced processing techniques, significantly enhances the identification of mineralization potential. For instance, Hegab et al. (2022) successfully employed ASTER alongside geophysical and GIS data analysis to detect gold-related alteration zones in the Um Balad area of Egypt's Eastern Desert, demonstrating the sensor's efficacy in arid environments where bedrock exposure facilitates spectral detection. Similarly, Aboelkhair et al. (2021) integrated airborne geophysical data with ASTER remote sensing to delineate potential mineralization zones in the Hamash area, South Eastern Desert, Egypt, highlighting the value of multi-source data fusion in reducing exploration uncertainty.

Beyond gold exploration, Kalkhoran et al. (2025) developed a hybrid discrete wavelet transform and median absolute deviation (DWT-2D/MAD) algorithm to optimize hydrothermal alteration mapping in porphyry copper systems, achieving improved detection of key alteration minerals including alunite, kaolinite, and muscovite. Furthermore, research by Chen et al. (2022) utilized ASTER and GF-5 satellite data to map hydrothermal alteration minerals in the Longtoushan Pb-Zn deposit in southwestern China, while Belgrano et al. (2022) produced a 5000 km² ASTER alteration map of the Oman–UAE ophiolite, demonstrating multispectral discrimination of spectrally similar hydrothermal minerals in mafic crust. These advancements underscore ASTER's continued relevance in modern mineral exploration, particularly when combined with machine learning approaches and integrated with geochemical and geophysical datasets to generate robust mineral predictive maps (Shebl et al., 2023; El-Qassas et al., 2023).

II. MATERIALS AND METHODS

A. The Study Area

Zamfara State, located in Nigeria's North-West geopolitical zone, covers 39,761 km² with Gusau as its capital and borders the Republic of Niger and several Nigerian states. Its topography is predominantly low-lying and gently undulating, reaching about 430 meters above sea level near Gusau. Geologically, the state is underlain almost entirely by two formations: the Precambrian Basement Complex, composed of crystalline rocks like gneiss and granite covering roughly 90% of the area, and the Cretaceous-to-Tertiary Gundumi Formation, consisting of clays, sandstones, and pebble beds that form a key artesian aquifer in the remaining 10%.

The spatial framework of this investigation was established by defining a precise geographic boundary to ZAmfara State (Figure 1). The spatial geometry of this feature collection was extracted to programmatically delineate the study region, establishing a consistent geographic coordinate envelope for the entire workflow.To optimize cloud-computing efficiency and manage memory allocation during large-scale raster calculations, the study region geometry was utilized as a hard spatial filter. By restricting data queries, pixel-by-pixel operations, and spatial reductions strictly to this coordinate envelope. The defined study area served as the spatial baseline for the entire dataset pipeline. All raw satellite swaths, intermediate calculated indices, and final outputs were clipped to this exact geometry. This rigorous spatial standardization minimized edge-effect anomalies along scene boundaries, prevented processing errors, and ensured that all final raster outputs maintained identical spatial extents.

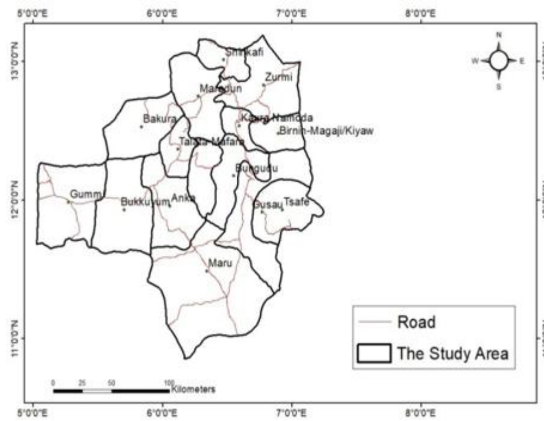

Fig 1.The Study Area

B. ASTER Data Acquisition and Preprocessing

Satellite data acquisition was conducted using the ASTER (Advanced Spaceborne Thermal Emission and Reflection Radiometer) L1T precision-terrain-corrected dataset. The image collection was filtered spatially to retain only those scenes intersecting the designated study region. To ensure high spectral fidelity and minimize atmospheric obstructions, a maximum cloud-cover threshold of 20% was enforced, and the temporal range was restricted to the dry-season months of November through March to minimize active vegetative canopy interference. A median pixel reducer was subsequently applied across the temporal stack to generate a single, cloud-free composite.

To convert the at-sensor radiance values to surface reflectance, a custom Dark Object Subtraction (DOS) atmospheric correction algorithm was implemented. The function isolated the Visible and Near-Infrared (VNIR) bands and identified the lowest pixel values within the study area using a minimum reduction at a scale of 1000 meters. Based on the physical assumption that deep water bodies or shadows should exhibit zero reflectance, these minimum values were designated as the atmospheric path radiance (haze offset) and were subtracted from each corresponding band. Values falling below zero post-subtraction were corrected to a floor value of zero to maintain physical validity. This preprocessing stage neutralized atmospheric scattering, restoring the true spectral signatures of the surface geology and establishing a reliable baseline for spectral profile analysis.

C. Spectral Mineral Index Calculation

Surface mineralogy mapping was executed by calculating diagnostic mineral indices using spectral band math on the preprocessed ASTER composite (Table 1). This methodology exploits the characteristic absorption and reflection features of different mineral groups within the VNIR and SWIR regions of the electromagnetic spectrum. By rationing specific bands, subtle absorption anomalies of the target minerals were enhanced while background noise from topographic shadows, soil moisture, and variable illumination was suppressed.The spectral calculations targeted 11 distinct alteration minerals and mineral groups, utilizing equations designed to isolate key absorption depths (Table 1). The resulting outputs from these expressions were single-band,

continuous-value rasters where higher digital numbers represented stronger spectral absorption features. Clay minerals (such as Kaolinite and Illite), Carbonates, and Sulfates are mapped using the Shortwave Infrared (SWIR) bands because these minerals possess diagnostic hydroxyl (O–H), aluminum-hydroxyl (Al–OH), and carbonate ($CO3^{2-}$) absorption features between 1.60 µm and 2.43 µm. Iron oxides (Hematite and Goethite) are mapped using the Visible and Near-Infrared (VNIR) bands, isolating distinct iron absorption features in the blue-green spectrum (0.52–0.60 µm) and high reflectance in the red-to-infrared spectrum (0.63–0.86 µm).

Table 1: ASTER Band Ratio Formulas for Mapping Hydrothermal Alteration Mineral

Target Mineral / Group	Mathematical Expression	ASTER Bands Used (Wavelength Regions)
Kaolinite	(B4 × B7) / (B5 × B6)	B4, B5, B6, B7 (SWIR)
Illite / Muscovite	(B4 + B6) / B5	B4, B5, B6 (SWIR)
Montmorillonite	(B4 × B6) / ($B5^2$)	B4, B5, B6 (SWIR)
Alunite / Pyrophyllite	(B7 / B5) × (B7 / B8)	B5, B7, B8 (SWIR)
Carbonates	(B6 × B9) / (B7 × B8)	B6, B7, B8, B9 (SWIR)
Chlorite / Epidote	(B7 + B9) / B8	B7, B8, B9 (SWIR)
Hematite	B2 / B1	B1, B2 (VNIR)
Goethite	B1 / B2	B1, B2 (VNIR)
Jarosite	B4 / B5	B4, B5 (SWIR)
Gypsum	(B4 + B6) / B5	B4, B5, B6 (SWIR)
Quartz	(B11 × B11) / (B10 × B12)	B10, B11, B12 (TIR)

III. RESULTS AND DISCUSSION

1. Kaolinite Distribution

The kaolinite distribution map reveals a distinct spatial pattern characterized by very high concentrations (2.02–2.23) predominantly in the southern regions, particularly around Maru and extending toward the southeastern boundaries of the study area (Figure2). Moderate to high values are also observed in the western Gummi area and isolated pockets near Gusau-Tsafe. This distribution pattern suggests strong argillic alteration zones, which typically form in the upper levels of hydrothermal systems under acidic conditions (Jellouli et al., 2025). The significance of these findings lies in the identification of potential epithermal mineralization targets, as kaolinite-rich zones often indicate the presence of precious metal deposits. The main strength of this mapping approach is the clear delineation of alteration intensity gradients, which can guide field exploration priorities. Furthermore, Bahrami et al. (2024) demonstrated that machine learning algorithms, particularly Support Vector Machines (SVM), achieve 85% accuracy in lithological mapping using ASTER data, suggesting that integrating such techniques could enhance the reliability of kaolinite detection in this study area.

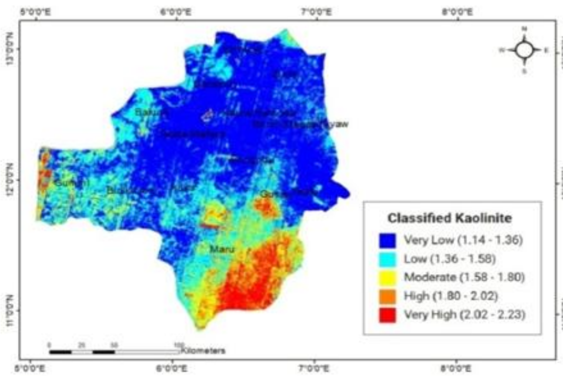

Figure 2. Classified Kaolinite

2. Illite-Muscovite Distribution

The result showed very high concentrations (2.95–3.14) of illite-muscovite in the southern Maru region and extending eastward (Figure 3). This overlap is geologically significant as illite-muscovite typically represents phyllic alteration, which forms at deeper levels and higher temperatures than argillic alteration, suggesting a superimposed hydrothermal system (Khaleghi et al., 2020). The presence of both minerals in proximity indicates potential zonation typical of porphyry copper systems. The findings align with Jellouli et al. (2025), who identified illite-muscovite as principal phyllic alteration minerals in Morocco's Anti-Atlas belt using Ninomiya indices and CEM classification, and their integration with Landsat-8 OLI data provided enhanced lithological discrimination.

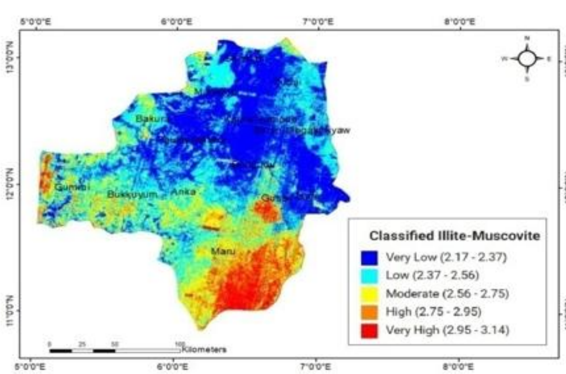

Figure3. Classified Illite-Muscovite

3. Montmorillonite Distribution

Montmorillonite displays a spatial pattern with very high values (2.10–2.33) in the southern Maru area and scattered high-value patches in the Gummi region (Figure 4). This smectite clay mineral indicates intermediate argillic alteration and its presence alongside kaolinite suggests variable pH conditions and fluid chemistry during alteration (Shebl et al., 2023). The significance of montmorillonite detection is its role as a pathfinder for base metal mineralization, particularly in epithermal environments. The mapping strength lies in identifying intermediate alteration zones that bridge argillic and propylitic assemblages. However, montmorillonite's variable hydration state can shift its spectral absorption features, potentially causing misclassification with other swelling clays. Moreover, Pereira et al. (2025) utilized PRISMA hyperspectral imagery with Google Earth Engine for multi-temporal mineral mapping and demonstrated discrimination of montmorillonite from other clay minerals, suggesting that future research in this area could benefit from hyperspectral sensors or advanced unmixing techniques.

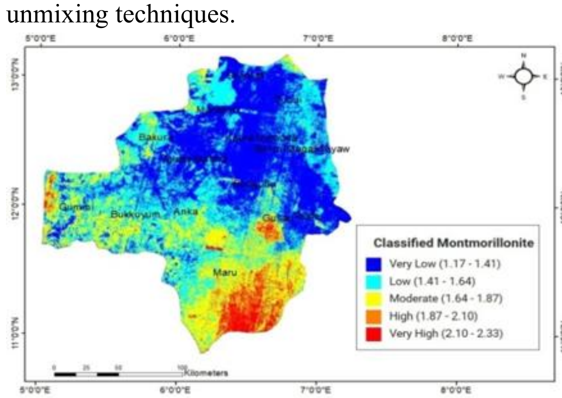

Figure 4. Classified Montmorillonite

4. Alunite-Pyrophyllite Distribution

The alunite-pyrophyllite map presents a more dispersed pattern compared to the clay minerals, with very high values (1.39–1.48) appearing as isolated hotspots rather than continuous zones. Notable concentrations occur near Kaura Namoda, scattered areas in the central Bungudu region, and the southern Maru area (Figure 5).This distribution is significant as alunite indicates advanced argillic alteration with strong acid sulfate conditions, often associated with high-sulfidation epithermal gold deposits (Jellouli et al., 2025). Pyrophyllite, conversely, indicates higher temperature phyllic to advanced argillic transition. The identification of these minerals is significant due to their potentially economic alteration assemblages.

Ahmadirouhani et al. (2018) successfully integrated SPOT-5 and ASTER data for alteration mineral mapping in Iran's Bajestan area, achieving better spatial resolution for alunite detection through data fusion. Similarly, Jellouli et al. (2025) distinguished alunite-rich zones using Ninomiya indices in Morocco, but their combined use of Maximum Likelihood and SVM classifiers provided higher overall accuracy (91.74%).

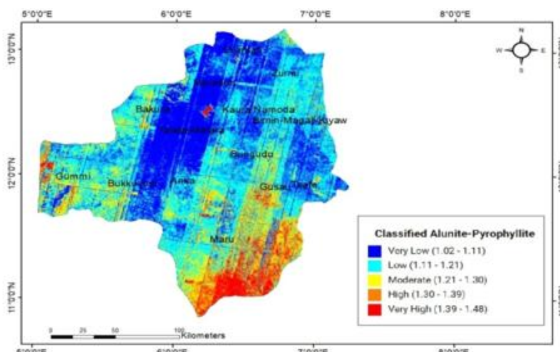

Figure 5. Classified Alunite-Pyrophyllite

5. Carbonates-MgOH Distribution

The carbonates-MgOH map exhibits an inverse pattern to most alteration minerals, with very high values (0.86–0.96) dominating the northern and central regions, particularly around Shinkafi, Zurmi, and Maradun, while the southern Maru area shows very low concentrations (Figure 6). This distribution is geologically significant as carbonate and Mg-OH bearing minerals (dolomite, calcite, chlorite, epidote) typically characterize propylitic alteration, the outermost and lowest temperature zone of porphyry systems (Bahrami et al., 2024). The clear zonation from south (argillic/phyllic) to north (propylitic) suggests a well-preserved hydrothermal system with distinct alteration zoning. The The identification of the propylitic halo helps define the overall system geometry. Detailed propylitic mineral mapping achieved by Khaleghi et al. (2020), who used laboratory spectra to specifically identify epidote-chlorite assemblages in Iran. Furthermore, Shebl et al. (2023) demonstrated that Relative Absorption Band Depth (RBD) techniques can distinguish Mg-Fe-OH minerals (chlorite-epidote) from carbonates using ASTER band ratios, suggesting that applying such indices could improve the specificity of the carbonate-MgOH mapping.

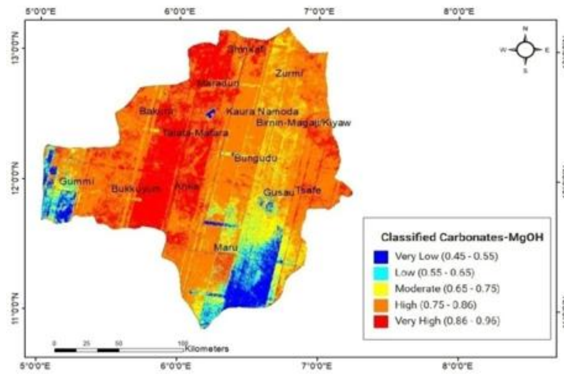

Figure 6 Classified Carbonates-MgOH

6. Chlorite-Epidote Distribution

The chlorite-epidote map shows very high values (1.83–1.91) across the entire study area, with only localized very low zones in the western Gummi area and southern Maru region (Figure 7). This extensive distribution pattern is geologically significant as chlorite-epidote represents propylitic alteration, but the near-complete coverage suggests either widespread low-grade metamorphism or potential spectral confusion with other ferromagnesian minerals. The identification of these minerals is crucial for defining the outer limits of hydrothermal systems and identifying potential host rocks for mineralization..Bahrami et al. (2024) noted that ASTER TIR bands have greater importance than SWIR bands for lithological mapping in their Sar-Cheshmeh study, suggesting that incorporating thermal infrared data could enhance chlorite-epidote discrimination in this research area.

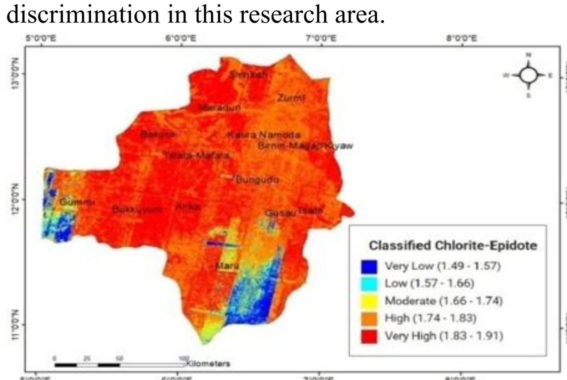

Figure 7. Classified Chlorite-Epidote

7. Hematite Distribution

The hematite map displays a heterogeneous pattern with very high concentrations (1.56–1.70) in the western Gummi area, northern Shinkafi region, and scattered patches throughout the central areas, while the southern Maru region shows predominantly low values (Figure 8). This distribution is significant as hematite is a primary iron oxide formed by oxidation of iron-bearing sulfides, commonly associated with gossans and weathered mineralized zones. The western high-values may indicate exposed iron-rich lithologies or supergene enrichment zones. Similarly, Abay et al., (2022) achieved precise ferric/ferrous iron oxide mapping in Ethiopia's Negash deposit using combined ASTER and Landsat 8 OLI data, with correlation coefficients of 0.85 and 0.81 for hematite and goethite respectively, demonstrating the value of multi-sensor approaches. Similarly, Moradpour et al. (2020) utilized Landsat-7 and ASTER imagery for iron skarn mineralization mapping in Iran, successfully distinguishing hematite, goethite, magnetite, and jarosite through integrated analysis.

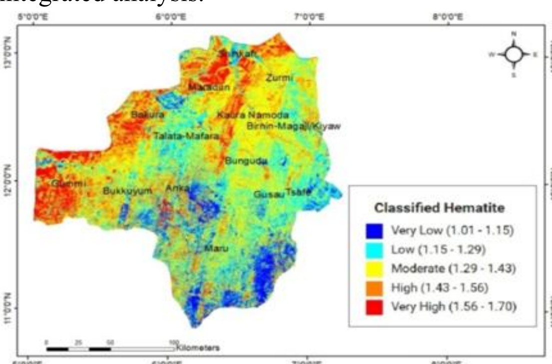

Figure 8. Classified Hematite

8. Goethite Distribution

The goethite map reveals very high concentrations (0.90–0.98) in the southern Maru region, with additional high-value areas in the central Bungudu and western Gummi regions (Figure 9). This pattern partially overlaps with hematite but shows distinct concentration in the south, suggesting variable oxidation conditions and water availability during iron oxide formation. Goethite typically forms in more humid, less acidic conditions than hematite, and its presence indicates ongoing or recent weathering processes (Khaleghi et al., 2020). The significance lies in identifying active weathering zones where supergene enrichment may be occurring. Similarly, Khaleghi et al. (2020), who used Directed Principal Component Analysis (DPCA) on Sentinel-2 and Landsat-8 data to specifically map goethite, jarosite, and hematite in Iran's Zamin-Hossein area. Furthermore, the research by Pereira et al. (2025) on multi-temporal mineral mapping using PRISMA hyperspectral imagery demonstrated that iron oxides and hydroxides (hematite, goethite, jarosite) can be temporally monitored for weathering progression.

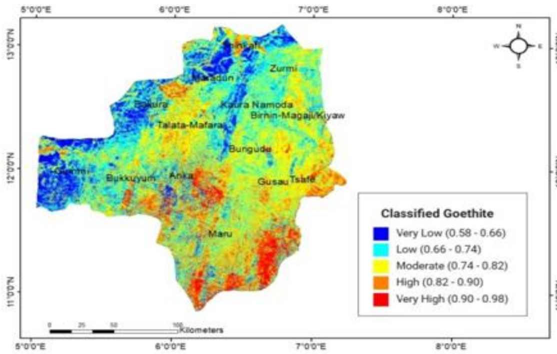

Figure 9. Classified Goethite-Limonite

9. Jarosite Distribution

The jarosite map shows very high values (1.74–1.90) concentrated in the southern Maru area, with moderate to high values extending through the central regions and isolated patches in the Gummi area (Figure 10). This distribution closely corresponds with the goethite pattern, which is geologically consistent as jarosite forms under strongly oxidizing, acidic conditions often associated with sulfide oxidation and goethite formation (Khaleghi et al., 2020). Jarosite is a particularly significant indicator mineral as it forms exclusively from sulfide oxidation, making it a direct pathfinder for underlying sulfide mineralization. The significance of this mapping is the identification of active acid-generating systems with high exploration potential. Moradpour et al. (2020) successfully mapped jarosite as part of iron skarn mineralization in Iran using ASTER band ratios, achieving validation through field spectrometry.

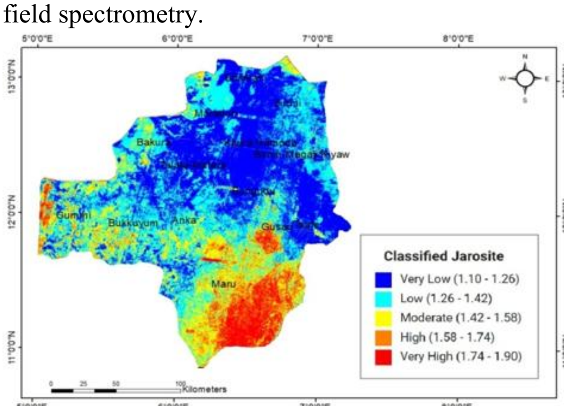

Figure 10 Classified Jarosite

10. Gypsum Distribution

The gypsum map exhibits very high values (2.95–3.14) predominantly in the southern Maru region, with additional high-value areas in the central Bungudu and Gusau-Tsafe regions, and very low values in the northern Shinkafi-Zurmi area (Figure 11). This distribution is geologically significant as gypsum forms through evaporation of sulfate-rich waters, often associated with oxidation of sulfide minerals or evaporite deposits (Rajendran & Nasir, 2021). Its presence in the same areas as jarosite and goethite suggests active sulfide oxidation with sulfate generation. The finding is significant because of the identification of sulfate-rich environments that may indicate sulfide mineralization at depth. Rajendran and Nasir (2021) also used ASTER SWIR and TIR bands to map gypsum deposits in Oman's Thumrait region with validation through field spectra and XRD analysis. Furthermore, Shuai et al. (2022) developed new spectral indices specifically for gypsum mapping using multi-seasonal ASTER data, demonstrating that seasonal variability affects gypsum detection and that targeted indices can improve mapping accuracy.

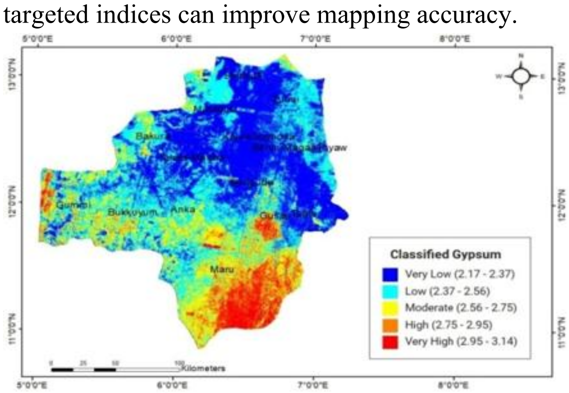

Figure 11. Classified Gypsum

11. Quartz Distribution

The quartz map shows a highly heterogeneous pattern with very high values (1.15–1.19) appearing as scattered linear and patchy features throughout the study area, particularly in the central and northern regions, while the southern Maru area shows predominantly low values (Figure 12). This distribution is significant as quartz is a resistant mineral that forms silicification zones, which can represent either hydrothermal alteration (phyllic/silicic) or simply quartz-rich host lithologies (Serbouti et al., 2022). The linear patterns may indicate structural controls on silicification., Serbouti et al. (2022) utilized Google Earth Engine with fused Landsat-8, ASTER, and Sentinel-2 data for lithological mapping in Morocco, employing machine learning algorithms Additionally, Pereira et al. (2025) used PRISMA hyperspectral data with GEE for multi-temporal mineral mapping, achieving quartz detection through its Si-OH features.

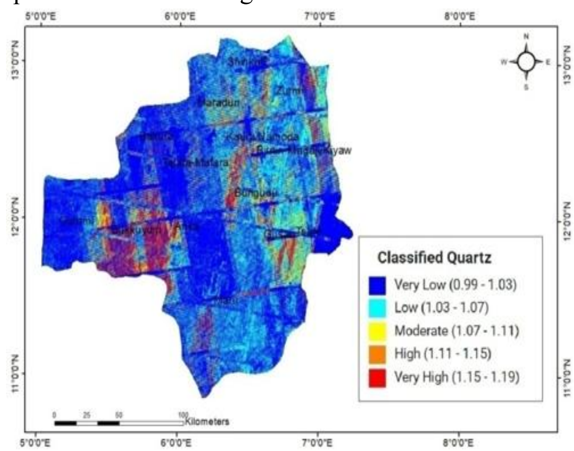

Figure 12. Classified Quartz

IV. CONCLUSION

This study has demonstrated the effectiveness of cloud-based multispectral remote sensing for reconnaissance-scale hydrothermal alteration mapping in Zamfara State, northwestern Nigeria By processing dry-season ASTER imagery within the Google Earth Engine platform and applying a Dark Object Subtraction atmospheric correction alongside eleven targeted band ratio expressions, the study successfully delineated a comprehensive suite of hydroxyl-, iron oxide-, carbonate-, and sulfate-bearing alteration minerals across the entire study area. This workflow required no local processing infrastructure or commercial software licensing, underscoring the value of cloud-based geospatial platforms as an accessible, repeatable, and cost-efficient reconnaissance tool for resource-constrained exploration settings.

The spatial results reveal a coherent and geologically meaningful alteration zonation consistent with a preserved hydrothermal system. Argillic and phyllic minerals, namely kaolinite, illite-muscovite, montmorillonite, alunite-pyrophyllite, jarosite, and goethite, are concentrated predominantly in the southern Maru region, coinciding spatially with the Anka and Maru schist belts, while propylitic assemblages dominated by carbonates and Mg-OH minerals prevail across the northern and central zones. This south-to-north gradient, from high-temperature acidic assemblages to a lower-temperature peripheral halo, rflects the classic zonation described for porphyry copper and epithermal gold systems worldwide. The co-occurrence of jarosite and gypsum in the southern zone further points to active sulfide oxidation, strengthening the interpretation that sulfide mineralization may persist at depth beneath the Maru schist belt corridor.

Beyond its immediate results, the study makes a methodological contribution by showing that a fully cloud-hosted ASTER workflow, requiring no proprietary desktop GIS software, can reproduce alteration patterns consistent with more resource-intensive multi-sensor and machine learning approaches This confirms the viability of Google Earth Engine as a first-pass reconnaissance tool that can meaningfully narrow down priority areas before costlier field-based or airborne surveys are commissioned.

Future work should integrate the derived alteration maps with complementary geophysical datasets, such as aeromagnetic and radiometric surveys, and with geochemical stream-sediment data, to reduce ambiguity in mineral discrimination and to better constrain subsurface mineralization at depth.

The significance of this research extends to multiple stakeholders. For the Nigerian Geological Survey Agency and other government mineral resource agencies, the study offers a low-cost, scalable template for regional-scale alteration reconnaissance that can inform national mineral resource inventories and licensing decisions. For mining and exploration companies, operating with limited exploration budgets, the delineated alteration zones provide a defensible, evidence-based basis for prioritizing ground follow-up and reducing exploration risk before committing capital to drilling. For policymakers and investors, the prospectivity of the Zamfara schist belt corridor strengthens the case for channeling investment toward a currently underexplored region, with potential downstream benefits for local employment and economic development, provided that any resulting exploration and extraction activity is guided by responsible environmental and social safeguards. Furthermore, the study reinforces the case for wider adoption of free, cloud-based satellite platforms across Nigerian and West African geoscience institutions, lowering the technical and financial barriers that have historically limited systematic mineral exploration in underexplored cratonic terrains.

REFERENCES

[1] Hegab, M. A. R., Mousa, S. E., Salem, S. M., Farag, K., & GabAllah, H. (2022). Gold-related alteration zones detection at the Um Balad area, Egyptian Eastern Desert, using remote sensing, geophysical, and GIS data analysis. Journal of African Earth Sciences, 196, 104715. https://doi.org/10.1016/j.jafrearsci.2022.104715

[2] Aboelkhair, H., Ibraheem, M., & Abou El-Magd, E. (2021). Integration of airborne geophysical and ASTER remotely sensed data for delineation and mapping the potential mineralization zones in Hamash area, South Eastern Desert, Egypt. Arabian Journal of Geosciences, 14, 1157. https://doi.org/10.1007/s12517-021-07471-y

[3] Kalkhoran, S. E., Ghannadpour, S. S., & Pour, A. B. (2025). Optimized hydrothermal alteration mapping in porphyry copper systems using a hybrid DWT-2D/MAD algorithm on ASTER satellite remote sensing imagery. Minerals, 15(6), 626. https://doi.org/10.3390/min15060626

[4] Chen, Q., Zhao, Z., Zhou, J., Zhu, R., Xia, J., Sun, T., & Chao, J. (2022). ASTER and GF-5 satellite data for mapping hydrothermal alteration minerals in the Longtoushan Pb-Zn deposit, SW China. Remote Sensing, 14(5), 1253. https://doi.org/10.3390/rs14051253

[5] Belgrano, T. M., Diamond, L. W., Novakovic, N., Hewson, R. D., Hecker, C. A., Wolf, R. C., Zieliński, L. D., Kuhn, R., & Gilgen, S. A. (2022). Multispectral discrimination of spectrally similar hydrothermal minerals in mafic crust: A 5000 km² ASTER alteration map of the Oman–UAE ophiolite. Remote Sensing of Environment, 280, 113211. https://doi.org/10.1016/j.rse.2022.113211

[6] Shebl, A., Abdellatif, M., Badawi, M., Dawoud, M., Csámer, Á., & others. (2023). Towards better delineation of hydrothermal alterations via multi-sensor remote sensing and airborne

geophysical data. Scientific Reports, 13, 7406. https://doi.org/10.1038/s41598-023-34531-y

[7] El-Qassas, R. A., Abu-Donia, A. M., & Omar, A. E. (2023). Delineation of hydrothermal alteration zones associated with mineral deposits, using remote sensing and airborne geophysics data: A case study of El-Bakriya area, Central Eastern Desert, Egypt. Acta Geodaetica et Geophysica, 58, 71–107. https://doi.org/10.1007/S40328-023-00405-Y

[8] Jellouli, A., Chakouri, M., Adiri, Z., El Hachimi, J., & Jari, A. (2025). Lithological and hydrothermal alteration mapping using Terra ASTER and Landsat-8 OLI multispectral data in the north-eastern border of Kerdous inlier, western Anti-Atlas belt, Morocco. Artificial Satellites, 60(1), 15–31. https://doi.org/10.2478/arsa-2025-0002

[9] Bahrami, H., Esmaeili, P., Homayouni, S., Pour, A. B., Chokmani, K., & Bahroudi, A. (2024). Machine learning-based lithological mapping from ASTER remote-sensing imagery. Minerals, 14(2), 202. https://doi.org/10.3390/min14020202

[10] Khaleghi, M., Ranjbar, H., Abedini, A., & Calagari, A. A. (2020). Synergetic use of the Sentinel-2, ASTER, and Landsat-8 data for hydrothermal alteration and iron oxide minerals mapping in a mine scale. Acta Geodynamica et Geomaterialia, 17(3), 311–328. https://doi.org/10.13168/AGG.2020.0023

[11] Pereira, I., García-Meléndez, E., Ferrer-Julià, M., van der Werff, H., Valenzuela, P., & Cruz, J. A. (2025). Multi-temporal mineral mapping in two torrential basins using PRISMA hyperspectral imagery. Remote Sensing, 17(15), 2582. https://doi.org/10.3390/rs17152582

[12] Ahmadirouhani, R., Karimpour, M. H., Rahimi, B., Malekzadeh-Shafaroudi, A., Pour, A. B., & Pradhan, B. (2018). Integration of SPOT-5 and ASTER satellite data for structural tracing and hydrothermal alteration mineral mapping: Implications for Cu–Au prospecting. International Journal of Image and Data Fusion, 9(3), 237–262. https://doi.org/10.1080/19479832.2018.1469548

[13] Abay, H. H., & Legesse, D. Suryabhagavan K. V. (2022). Mapping of ferric (Fe3+) and ferrous (Fe2+) iron oxides distribution using ASTER and Landsat 8 OLI data, in Negash Lateritic iron deposit, Northern Ethiopia. Geology, Ecology, and Landscapes, 8(1), 223–240. https://doi.org/10.1080/24749508.2022.2130556

[14] Moradpour, H., Rostami Paydar, G., Pour, A. B., Valizadeh Kamran, K., Feizizadeh, B., Muslim, A. M., & Hossain, M. S. (2020). Landsat-7 and ASTER remote sensing satellite imagery for identification of iron skarn mineralization in metamorphic regions. Geocarto International, 37(26), 14413–14433. https://doi.org/10.1080/10106049.2020.1810327

[15] Rajendran, S., & Nasir, S. (2021). ASTER mapping of gypsum deposits of Thumrait region of southern Oman. Resource Geology, 71(1), 41–62. https://doi.org/10.1111/rge.12245

[16] Shuai, S., Zhang, Z., Lv, X., & Hao, L. (2022). Assessment of new spectral indices and multi-seasonal ASTER data for gypsum mapping. Carbonates and Evaporites, 37(2), 75. https://doi.org/10.1007/s13146-022-00775-4

[17] Serbouti, I., Raji, M., Hakdaoui, M., El Kamel, F., Pradhan, B., Gite, S., Alamri, A., Maulud, K. N. A., & Dikshit, A. (2022). Improved lithological map of large complex semi-arid regions using spectral and textural datasets within Google Earth Engine and fused machine learning multi-classifiers. Remote Sensing, 14(21), 5498. https://doi.org/10.3390/rs14215498